

# ETHANOL POOL FIRE ON A ONE-METER TEST TRAY – VALIDATION OF CFD RESULTS

Robert Cherbański<sup>1\*</sup>, Leszek Rudniak<sup>1</sup>, Piotr Machniewski<sup>1</sup>, Eugeniusz Molga<sup>1</sup>,  
Jarosław Tępiński<sup>2</sup>, Wojciech Klapsa<sup>2</sup>, Piotr Lesiak<sup>2</sup>

<sup>1</sup>Warsaw University of Technology, Faculty of Chemical and Process Engineering,  
ul. Waryńskiego 1, 00-645 Warsaw, Poland

<sup>2</sup>Scientific and Research Centre for Fire Protection of the National Research Institute,  
ul. Nadwiślańska 213, 05-420 Józefów, Poland

The ethanol fire hazards will become more frequent due to the new established targets for the consumption of renewable energy sources. With this in mind, this paper aims to widen the current knowledge on CFD modelling of such a fire. As previous works rely heavily on the data of small pool fire diameters (below 1 m), this research deals with ethanol pool fire on a one-meter test tray, using our own experimental data. A mathematical model was developed and solved using a commercial CFD package (ANSYS Fluent). A new hybrid RANS-LES (SBES) model was employed to calculate turbulent stresses. Generally, the simulation results showed a good fit with the experimental results for flame temperatures at different elevations. In particular, a minor discrepancy was only observed for the top thermocouple (1.9 m above the tray). The flame heights computed with the CFD model were on average higher than the experimental one. Good agreement was observed for the radiative fraction and the axial temperature profile on the plume centreline. The latter showed an almost perfect fit between the temperature profiles obtained from CFD simulations and those calculated from the plume law for temperature.

**Keywords:** pool fire, ethanol, CFD, large-scale, SBES

## 1. INTRODUCTION

There are many examples of fires with dramatic consequences in the past, such as the fire of L’Innovation department store in Brussels in 1967, which killed 251 people and injured 62, and the fire at the Cinq Sept club in Saint-Laurent-du-Pont in France in 1970, in which 146 people died (Cajot et al., 2008). Although the number of global fire fatalities has been declining since 2001 (Brushlinsky et al., 2020), there is still a need to further improve safety in different places, as for example: chemical installations, tunnels, shopping and office centres, underground metro stations and garages.

The Renewable Energy Directive II has introduced new targets for renewable energy source consumption by 2030 (Directive 2009/28/EC, 2009). According to this directive, an increased 14% sub-target for transport

\* Corresponding author, e-mail: robert.cherbanski@pw.edu.pl

<https://journals.pan.pl/cpe>



has been set. Given that ethanol is recognized as one of the most important biofuels, its storage capacity will increase.

One of the most spectacular accidents was the 4000 m<sup>3</sup> ethanol tank fire in Port Kembla (Australia) in January 2004 (Marlair et al., 2009). The investigations into ethanol fires are also important from fire safety perspective in alcoholic beverage industry and retail stores (Hakkarainen et al., 2021). The fire safety issues may also arise due to common usage and storage of concentrated alcohol solutions used as a disinfectant for sanitary purposes, especially during the COVID-19 pandemic. Overall, the list of accidents and incidents that have occurred at ethanol fuel plants is very long (Calvo Olivares et al., 2015; Marlair et al., 2009). As a result, an ethanol fire has to be considered in the various safety analyses in the biofuel industry.

CFD simulations of a pool fire, in addition to various experimental techniques, can provide very valuable information regarding the temperature field in the vicinity of a fire. However, CFD approach applied to fire modelling remains a major challenge due to the complexity of fire phenomena. In addition, high computing power is usually required, especially when such simulations reflect dynamic scenarios in large-scale facilities. A separate issue is the accuracy of modelling results, which is a consequence of adopted simplifications, which at the same time allow to shorten the calculation time.

A pool fire on a test tray is a typical setup used in various experimental studies. Such an arrangement was employed in many previous studies to test the results of CFD modelling. For instance, Schälke et al. (2012) carried out the CFD simulations of n-hexane pool fire with a diameter of 5 cm. The computations were performed using the commercial CFD package, ANSYS Fluent. Turbulence was modelled using Large Eddy Simulation (LES) model with the Smagorinsky–Lilly sub-mesh viscosity model while combustion was modelled using the probability density function with laminar flamelets. A simplified mechanism of combustion was considered, which contained 20 compounds and 42 chemical reactions. Given that the contribution of thermal radiation in the total heat flux and the soot emissivity were low, neither thermal radiation nor soot production was taken into account in the proposed mathematical model. For the discretization of computational domain, a non-structural hexahedral mesh consisting of  $2 \times 10^6$  elements was generated. The validation of the mathematical model was performed by comparing the CFD and experimental results concerning the axial concentration profiles and the radial profiles of average temperatures at three different heights above the liquid surface. A comparison of the calculated and measured concentrations showed that the mean square deviation was 6.4%. In turn, a comparison of the calculated and measured interferometric temperatures showed that the average temperature difference was  $\Delta T \approx 13.5$  K.

Rengel et al. (2018) conducted the CFD simulations of gasoline and diesel pool fires with diameters of 1.5, 3, 4, 5 and 6 m. Two computer codes were compared: Fire Dynamics Simulator (FDS) and Flame Accelerator Simulator Fire (FLACS-Fire), and the main strengths and weaknesses of both CFD tools were indicated. Turbulence was modelled using  $k$ - $\varepsilon$  model in the case of FLACS-Fire and LES with the Deardorff sub-mesh turbulent viscosity model in the case of FDS software. Although the modelling took into account the evaporation of gasoline and diesel fuels, different techniques for producing and igniting flammable fuel vapours were applied. Combustion phenomenon was described by the Eddy Dissipation model. A simple model of soot formation was also introduced in the modelling, assuming constant values of the fuel-to-soot conversion factors. Thermal radiation and wind force were considered as well. Various numerical grids were tested with a number of elements ranging from 730 000 to 2 640 000 for FDS and from 180 000 to 1 140 000 for FLACS-Fire. The CFD results were compared with experimental results with regard to: flame temperatures, burning rates, heat fluxes, flame heights, flame areas and surface emissive powers.

Attar et al. (2013) carried out the CFD simulations of pool fires of gasoline, kerosene and peroxide (tert-butyl peroxybenzoate, TBPB) with diameters of 0.06, 0.11 and 0.18 m. The numerical simulations were performed using ANSYS Fluent. Reynolds Stress Model (RSM) and LES were used to model turbulence while Eddy Dissipation model was used for the mathematical description of combustion. Thermal radiation

and soot formation were modelled using Discrete Ordinate (DO) model and Khan and Greeves one-step empirical model, respectively. The calculations were performed in the three-dimensional domain. The numerical grid contained approximately 315 000 elements. The CFD results were compared with the experimental results based on the axial temperature profiles and the intensity of thermal radiation.

[Snegirev et al. \(2018\)](#) presented the CFD results of methane and heptane pool fires with diameters of 0.38 m and 0.3 m, respectively. The calculations were carried out in ANSYS Fluent. Turbulence was modelled using LES with the Smagorinsky–Lilly sub-mesh turbulent viscosity model. Combustion was described by Eddy Dissipation model and the flamelet model with the simplified reaction mechanism containing 29 compounds and 52 chemical reactions. Thermal radiation was included in the modelling using DO model. Particular attention was paid to the soot formation. The following models were compared: one-stage ([Khan and Greeves, 1974](#)), two-stage ([Tesner et al., 1971](#)) and the Moss–Brooks model in combination with three models of soot oxidation ([Fenimore and Jones, 1967](#); [Lee et al., 1962](#); and [Magnussen and Hjertager, 1977](#)). The Moss–Brooks model was extended with the soot oxidation model and calibrated to heptane.

[Gore et al. \(2007\)](#) reported that radiation losses to the surroundings contribute to 17–20% of the total heat of combustion in the case of ethanol, hexanol and methanol pool fires, and 31–34% in the case of soothing fuels (heptane, toluene, methyl methacrylate). The results were based on the measurements of burning rate and radiative heat flux around the flames (7 cm Pyrex container and 30 cm stainless steel pan were used in the experiment). Similar findings were reported by [Chan Kim et al. \(2019\)](#) who measured radiative and total heat flux in steadily burning methanol, ethanol or acetone pool fires (0.3 m stainless steel burner). The authors found that convection in the plume represented 68–78% of the fire's total energy, thus, exceeding radiative emission to the surroundings. However, radiation was the dominant mechanism for heat feedback transferred to the fuel surface in all the test cases (e.g. 84% in the case of ethanol pool fire).

While the problem of ethanol fires is becoming increasingly important nowadays, to the best of our knowledge, there are few papers that address this topic in small ([Falkenstein-Smith et al., 2021](#); [Fischer et al., 1987](#); [Hamins et al., 1991](#)) and large ([Sjöström et al., 2015a, 2015b](#)) scale experiments. What is surprising is the fact that CFD modelling of ethanol pool fires is the subject only of a few articles ([Chotzoglou et al., 2019](#); [Ebrahim Zadeh et al., 2016](#); [Maragkos and Merci, 2021](#); [Steinhaus et al., 2007](#); [Stewart et al., 2021](#)). Further, they consider pool fires with rather small diameters, i.e. less than 1 m. As a result, this paper aims to validate CFD modelling results of ethanol pool fire on a one-meter test tray using our own experimental data. Furthermore, the Stress-Blended Eddy Simulation (SBES) model was used for the calculation of turbulent stresses. As this hybrid RANS-LES model has not been used previously to model an ethanol pool fire, we decided to verify it in the calculations to fill this gap.

## 2. EXPERIMENTAL

Ethanol dehydrated completely denatured (ESOLL, Poland) according to WE3199/93 was used in all experiments. Table 1 details the composition of ethanol mixture.

Table 1. Specification of the ethanol mixture

Chemical composition	Units	Limits
Ethanol dehydrated	wt. %	max. 98.0
Isopropanol	wt. %	min. 1.0
Methyl ethyl ketone	wt. %	min. 1.0
Denatonium benzoate	wt. %	min. 0.001

The ethanol pool fire tests were carried out on a test stand (Fig. 1) located in the Training Center in Pionki of the Provincial Headquarters of the State Fire Service in Warsaw. The temperatures in the axial position of a test tray and flame height were measured during these tests.



Fig. 1. Pool fire test stand: T1–T3 – thermocouples

Figure 2 shows a technical drawing of a tray with a test chamber diameter of 100 cm. During the tests, 9 litres of ethanol were used, which filled the test chamber to a height of 1.2 cm. There was also a ring shaped chamber filled with water to cool the tray.

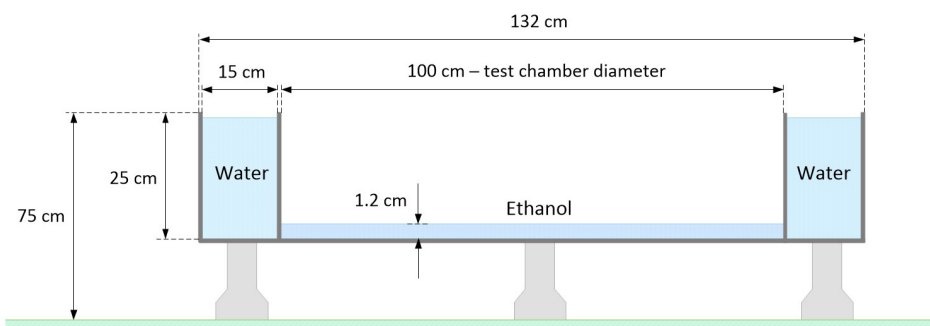


Fig. 2. Technical drawing of a test tray

The temperature measuring system consisted of 3 thermocouples (N-type, class 1 according to EN 60584-2) with compensation cables, National Instruments controller type NI cDAQ 9174 equipped with the NI 9214 module with the TB-9214 connection block, and a computer with the NI SignalExpress 2015 software.

The N-type thermocouples (NiCrSi–NiSi) were chosen because they can withstand temperatures up to 1200 °C. Please note that the maximum temperature in our experiments did not exceed 1000 °C. The thermocouples have a very good linearity of temperature measurement, good sensitivity and thermal stability. The choice of the thermocouple and its diameter was consulted with the manufacturer. As a result, the thermocouples with a larger diameter than the standard ones were used during the tests. The thermocouples were checked by the manufacturer and delivered with the appropriate manufacturer's declaration. The thermocouples were also tested in the laboratory and successfully passed the tests. The permissible measurement error resulting from the EN 60584-1 standard for this sensor and for this type of tests can be considered as insignificant. As a result, no correction factors were introduced.

Using a heat-resistant steel stand (Fig. 3), three N-type thermocouples were mounted at the heights of 50 cm, 130 cm and 190 cm above the bottom surface of the test tray.

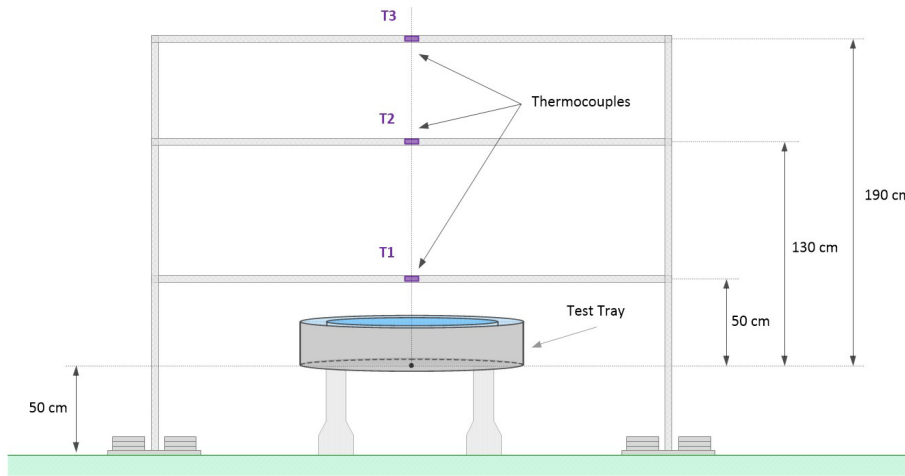


Fig. 3. Heat-resistant steel stand for mounting the N-type thermocouples

Table 2 shows the weather conditions that occurred during the pool fire tests.

Table 2. Weather conditions during the pool fire tests

Wind direction	Wind speed [m/s]	Temperature [°C]	Humidity [%]	Pressure [hPa]	Cloudy
NE/E	0.4	31	46	1017.4	Low

Flame height was estimated on the basis of video recordings. Prior to experiments, a measuring stick with graduations of specific lengths was placed near the test tray to calibrate the height on the video recording (Fig. 4). The estimated average flame height during the test was 148 cm.

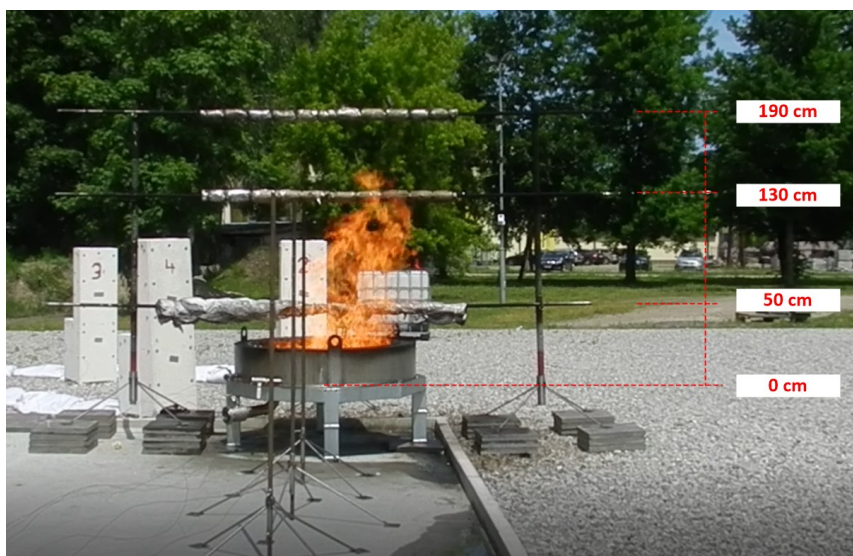


Fig. 4. Stand during pool fire research

### 3. THEORY

The CFD simulation of fire is based on the numerical solution of differential balance equations. In order to simulate pool fires, which typically occur in turbulent flow regime, the following balance equations are required: mass, momentum, components and energy.

#### 3.1. Governing equations

##### 3.1.1. Mass balance (continuity equation)

The mass balance or continuity equation can be written as follows

$$\frac{\partial \rho}{\partial t} + \nabla \cdot (\rho \vec{v}) = S_m \quad (1)$$

where  $\rho$  is the density,  $\vec{v}$  is the velocity vector,  $S_m$  is the source term in the mass balance.

##### 3.1.2. Momentum balance

The momentum balance equation in vector notation has the following form

$$\frac{\partial (\rho \vec{v})}{\partial t} + \nabla \cdot (\rho \vec{v} \vec{v}) = -\nabla p + \nabla \cdot (\overline{\overline{\tau}}) + \rho \vec{g} + \vec{F} \quad (2)$$

where:  $p$  is the static pressure,  $\rho \vec{g}$  and  $\vec{F}$  are the gravitational body force and external body forces, respectively. The stress tensor,  $\overline{\overline{\tau}}$ , is defined as follows

$$\overline{\overline{\tau}} = \mu \left[ (\nabla \vec{v} + \nabla \vec{v}^T) - \frac{2}{3} \nabla \cdot \vec{v} I \right] \quad (3)$$

where:  $\mu$  is the molecular viscosity and  $I$  is the unit tensor.

Equation (2) is valid in the laminar regime. In the turbulent regime, a modification of the above equations is required. According to Reynolds averaging, the solution variables in the instantaneous momentum balance are divided into the mean and fluctuating components as

$$\eta = \overline{\eta} + \eta' \quad (4)$$

where:  $\eta$  is the instantaneous value of the corresponding variable ( $u$ ,  $v$ ,  $w$ ,  $p$ ),  $\eta'$  is the fluctuating value of the corresponding variable,  $\overline{\eta}$  is the mean value of the corresponding variable that is defined as

$$\overline{\eta} = \frac{1}{\Delta t} \int_t^{t+\Delta t} \eta dt \quad (5)$$

After such averaging (Reynolds-averaged Navier–Stokes, RANS) of Equations (1) and (2), they can be transformed into the following form (index notation, the overbar over mean velocity symbol is omitted in subsequent equations).

$$\rho \left( \frac{\partial u_i}{\partial t} + u_j \frac{\partial u_i}{\partial x_j} \right) = -\frac{\partial p}{\partial x_i} + \frac{\partial}{\partial x_j} \left( \mu \frac{\partial u_i}{\partial x_j} \right) + \rho g_i + \frac{\partial (-\rho \overline{u'_i u'_j})}{\partial x_j} \quad (6)$$

The Reynolds stresses ( $-\rho \overline{u'_i u'_j}$ ) in Equation (6) are modelled employing the Boussinesq hypothesis as follows

$$-\rho \overline{u'_i u'_j} = \mu_t \left( \frac{\partial u_i}{\partial x_j} + \frac{\partial u_j}{\partial x_i} \right) - \frac{2}{3} \left( \mu_t \frac{\partial u_k}{\partial x_k} + \rho k \right) \delta_{ij} \quad (7)$$

where  $\mu_t$  is the turbulent viscosity, which is calculated in this work using the Generalized  $k$ - $\omega$  (GEKO) model as follows

$$\mu_t = \rho \frac{k}{\max(\omega, S/C_{\text{REAL}})} \quad (8)$$

where  $C_{\text{REAL}} = 0.577$ .

The GEKO extension of the  $k$ - $\omega$  model introduces additional parameters allowing for the calibration of this model for near-wall flows without worsening its predictions for other flows (ANSYS Inc., 2021).

The turbulence kinetic energy  $k$  and the specific turbulence kinetic energy dissipation rate  $\omega$  occurring in Equation (8) are calculated by solving the following transport equations

$$\frac{\partial(\rho k)}{\partial t} + \frac{\partial(\rho u_j k)}{\partial x_j} = P_k - \rho C_{\mu} k \omega + \frac{\partial}{\partial x_j} \left[ \left( \mu + \frac{\mu_t}{\sigma_k} \right) \frac{\partial k}{\partial x_j} \right] \quad (9)$$

$$\frac{\partial(\rho \omega)}{\partial t} + \frac{\partial(\rho u_j \omega)}{\partial x_j} = C_{\omega 1} F_1 \frac{\omega}{k} P_k - C_{\omega 2} F_2 \rho \omega^2 + F_3 \frac{2}{\sigma_{\omega}} \frac{\rho}{\omega} \frac{\partial k}{\partial x_j} \frac{\partial \omega}{\partial x_j} + \frac{\partial}{\partial x_j} \left[ \left( \mu + \frac{\mu_t}{\sigma_{\omega}} \right) \frac{\partial \omega}{\partial x_j} \right] \quad (10)$$

where  $F_1, F_2, F_3$  are the functions containing six parameters:  $C_{\text{SEP}}, C_{\text{MIX}}, C_{\text{NW}}, C_{\text{JET}}, C_{\text{CORNER}}$  and  $C_{\text{CURVE}}$ .

The coefficient  $C_{\text{SEP}}$  is used for adjusting separation prediction for boundary layers. The coefficient  $C_{\text{NW}}$  is introduced to impact mostly the inner part of wall boundary layers without any impact on free shear flows. While the parameters  $C_{\text{SEP}}$  and  $C_{\text{NW}}$  affect boundary layers,  $C_{\text{MIX}}$  and  $C_{\text{JET}}$  are designed for free shear flows (the blending function introduced in the model deactivates these coefficients in the boundary layer). The following default values of these coefficients were used:  $C_{\text{SEP}} = 1.75$ ,  $C_{\text{MIX}} = 0.3$ ,  $C_{\text{NW}} = 0.5$  and  $C_{\text{JET}} = 0.9$ , which roughly correspond to the  $k$ - $\omega$  SST model (the values of  $C_{\text{SEP}} = 1.0$ ,  $C_{\text{MIX}} = 0$ ,  $C_{\text{NW}} = 1$  correspond to the  $k$ - $\omega$  model) (ANSYS Inc., 2021).

Turbulent flows are characterized by eddies with a wide range of lengths and time scales. The largest eddies have a size comparable to the characteristic length of the averaged flow. In turn, the smallest eddies are responsible for the dissipation of turbulence kinetic energy.

Theoretically, the entire range of eddy sizes can be numerically modelled using the Direct Numerical Simulations (DNS) method. However, the computational cost is very high due to the requirements for mesh size and time step. For example, the number of elements for fully-developed turbulent flow can be as high as a billion or more. LES is an alternative method to solve this problem. In this method, large eddies are calculated directly, whereas small eddies are modelled. A filter function determines the scale of the smallest eddies that can be directly simulated by solving the filtered Navier–Stokes equation. This is a very important feature of the LES model. The filtering can be carried out in the wave-number space or in the physical space. In the latter case the filtering function filters out the eddies having scales smaller than the mesh size used in the numerical computations.

Eddies smaller than the size of the computational grid are the source of the so-called subgrid-scale stresses that need appropriate modelling. This requires the use of the filtering function  $G(x, x')$  which transforms any quantity  $\varphi(x)$  characterizing the turbulence field into its filtered component determined during the numerical solution of the system of turbulent motion equations. The filtering procedure can be written as a convolution operation, which for the simple 1D case takes the following form:

$$\overline{\varphi}(x) = \int_D \varphi(x') G(x, x') dx' \quad (11)$$

where

$$G(\mathbf{x}, \mathbf{x}') = \begin{cases} 1/V & \text{for } \mathbf{x}' \in \nu \\ 0 & \text{for } \mathbf{x}' \notin \nu \end{cases} \quad (12)$$

Thus, the filtered variable can be calculated from the following relationship

$$\bar{\varphi}(\mathbf{x}) = \frac{1}{V} \int_{\nu} \varphi(\mathbf{x}') \, d\mathbf{x}', \quad \mathbf{x}' \in V \quad (13)$$

The LES method in ANSYS Fluent uses the mesh cell size as the filter. As a result, the following form of filtered Navier–Stokes equations is obtained

$$\frac{\partial \bar{u}_i}{\partial t} + \frac{\partial \bar{u}_i \bar{u}_j}{\partial x_j} = -\frac{1}{\rho} \frac{\partial \bar{p}}{\partial x_i} + \frac{\partial}{\partial x_j} \left( \nu \frac{\partial \bar{u}_i}{\partial x_j} \right) - \frac{\partial \tau_{ij}}{\partial x_j} \quad (14)$$

where

$$\tau_{ij} = \overline{u_i u_j} - \bar{u}_i \bar{u}_j \quad (15)$$

is the sub-grid stress tensor which should be approximated using an appropriate model. The role of this model is very important as approx. 20% of the energy of turbulent fluctuations should be contained in the correctly modelled sub-grid stresses. LES model takes advantage of one of the important features of turbulence, which consists in modelling of the fine scales with isotropy of the eddy structure while numerically solving the anisotropic fields of large eddies. However, the most important advantage of the LES model is a significant reduction in computational cost compared to the DNS method.

Using the Boussinesq hypothesis, the sub-grid stresses can be expressed using the turbulent viscosity related to the sub-grid scale as

$$\tau_{ij}^{\text{LES}} = \tau_{ij} - \frac{1}{3} \tau_{kk} \delta_{ij} = -2\mu_t \bar{S}_{ij} \quad (16)$$

According to the Smagorinsky–Lilly model, the sub-grid turbulent viscosity can be calculated as follows

$$\mu_t = \rho L_s^2 |\bar{S}| = \rho L_s^2 \sqrt{2\bar{S}_{ij} \bar{S}_{ij}} \quad (17)$$

where  $L_s = \min(\kappa d, C_s \Delta)$ .

In this work, the Stress-Blended Eddy Simulation (SBES) model was also used (ANSYS Inc., 2021). SBES is a hybrid approach that combines both LES and RANS models for the calculation of turbulent stresses. The turbulent stresses are calculated using a blending function,  $f_{\text{SBES}}$ , as follows

$$\tau_{ij}^{\text{SBES}} = f_{\text{SBES}} \cdot \tau_{ij}^{\text{RANS}} + (1 - f_{\text{SBES}}) \cdot \tau_{ij}^{\text{LES}} \quad (18)$$

where  $\tau_{ij}^{\text{RANS}}$  is the contribution of the RANS model and  $\tau_{ij}^{\text{LES}}$  is the contribution of the LES model.

The RANS model is mainly used in the boundary layer and in the zones of intensive mixing (then  $f_{\text{SBES}} = 1$ ) while the LES model is used in the remaining area (where  $f_{\text{SBES}} = 0$ ).

### 3.2. Combustion model

The local mass fractions of the modelled species: ethanol, oxygen, carbon dioxide, water were calculated by solving conservation equations for chemical species in the following form

$$\frac{\partial}{\partial t} (\rho Y_j) + \nabla \cdot (\rho \vec{v} Y_j) = -\nabla \cdot \vec{J}_j + R_j \quad (19)$$

where  $Y_j$  is the mass fraction of species  $j$ ,  $R_j$  is the net rate of production of species  $j$  by combustion,  $\vec{J}_j$  is the mass diffusion in turbulent flow which is calculated as follows

$$\vec{J}_j = - \left( \rho D_{j,m} + \frac{\mu_t}{Sc_t} \right) \nabla Y_j - D_{T,j} \frac{\nabla T}{T} \quad (20)$$

where  $D_{j,m}$  is the mass diffusion coefficient for species  $j$  in the mixture,  $D_{T,j}$  is the thermal diffusion coefficient,  $Sc_t$  is the turbulent Schmidt number,  $\mu_t$  is the turbulent viscosity calculated from the appropriate models (see Equations (8) and (17)).

In ANSYS Fluent, Equation (19) is solved for  $N - 1$  species (4 in our case) to minimize numerical error. The  $N^{\text{th}}$  species ( $N_2$  in our case as air is the oxidizer) is calculated simply as

$$Y_N = 1 - \sum_1^{N-1} Y_j \quad (21)$$

Given that most fuels burn very fast and that the mixing rate of fuel with air is usually the bottleneck of the entire process in the non-premixed combustion, the mathematical modelling of such cases can be simplified assuming that the rate of combustion is infinitely fast, i.e. fuel reacts immediately after mixing with an oxidant. Such an approach was proposed in the Eddy Dissipation Model by Magnussen and Hjertager (1977). In the model, the net rate of production of species  $j$  due to reaction  $r$  is governed by the smaller of Equations (22) and (23).

$$R_{j,r} = \nu'_{j,r} M_{w,j} A \rho \frac{\varepsilon}{k} \min \left( \frac{Y_R}{M_{w,r} \nu'_{R,r}} \right) \quad (22)$$

$$R_{j,r} = \nu'_{j,r} M_{w,j} A B \rho \frac{\varepsilon}{k} \frac{\sum_P Y_P}{\sum_j M_{w,j} \nu''_{j,r}} \quad (23)$$

where  $Y_R$  is the mass fraction of a reactant  $R$ ,  $Y_P$  is the mass fraction of a product species  $P$ ,  $A$  is an empirical constant equal to 4.0,  $B$  is an empirical constant equal to 0.5. Note that the reaction rate depends on the presence of turbulence, i.e.  $k/\varepsilon > 0$  and an ignition source is not required.

In the case of the LES model, the characteristic turbulent mixing rate ( $\varepsilon/k$ ) is replaced by the sub-grid scale mixing rate  $\sqrt{2 S_{ij} S_{ij}}$ , where  $S_{ij} = \frac{1}{2} \left( \frac{\partial u_i}{\partial x_j} + \frac{\partial u_j}{\partial x_i} \right)$  is the strain rate tensor.

### 3.3. Energy balance

In addition to the mass, momentum and component balance, the energy balance is also required to model pool fires. The most frequently used form of the energy balance equation is determined by Equation (24).

$$\frac{\partial(\rho E)}{\partial t} + \nabla \cdot [\vec{v}(\rho E + P)] = \nabla \cdot \left[ k_{\text{eff}} \nabla T - \sum_j h_j J_j + (\bar{\tau}_{\text{eff}} \cdot \vec{v}) \right] + S_h \quad (24)$$

where  $k_{\text{eff}}$  is the effective conductivity ( $k_{\text{eff}} = k + k_t$ , where  $k_t$  is the turbulent thermal conductivity, defined according to the turbulence model being used),  $J_j$  is the diffusion flux of species  $j$ ,  $S_h$  is an internal source of heat resulting from, for example, chemical reactions.

In Equation (24), the total energy is defined by the following equation

$$E = h - \frac{p}{\rho} + \frac{v^2}{2} \quad (25)$$

where sensible enthalpy  $h$  is defined for ideal gases as

$$h = \sum_j Y_j h_j \quad (26)$$

where  $Y_j$  is the mass fraction of species  $j$ , and  $h_j = \int_{T_{\text{ref}}}^T c_{p,j} dT$ .

Modelling of pool fires also requires thermal radiation to be included in the energy balance equation. In this work, thermal radiation was simulated using Discrete Ordinate Model.

$$\nabla \cdot (I(\vec{r}, \vec{s}) \vec{s}) + (\alpha + \sigma_s) I(\vec{r}, \vec{s}) = \alpha n^2 \frac{\sigma T^4}{\pi} + \frac{\sigma_s}{4\pi} \int_0^{4\pi} I(\vec{r}, \vec{s}') \Phi(\vec{s}, \vec{s}') d\Omega \quad (27)$$

where  $\vec{r}$  is the position vector,  $\vec{s}$  is the direction vector,  $\vec{s}'$  is the scattering direction vector,  $\alpha$  is the absorption coefficient,  $\sigma_s$  is the scattering coefficient,  $\sigma$  is the Stefan–Boltzmann constant,  $I$  is the radiation intensity,  $T$  is the local temperature,  $\Phi$  is the phase function,  $\Omega$  is the solid angle.

### 3.4. Computational domain and boundary conditions

The computational domain was defined in 3D geometry with the axis origin located in the axis of the test tray at the height of its bottom, i.e. 0.5 m from the lower edge of the domain. Table 3 details the dimensions of the computational domain.

Table 3. The dimensions of the computational domain in cylindrical coordinates

Height	25.75 m
Radius	10.00 m
Height of the test tray above ground	0.5 m

Figure 5 shows a part of the computational mesh adjacent to the test tray filled with ethanol. The CFD model was simplified by assuming that ethanol fills the inside of the tray and the liquid surface is at the edge of the tray.

The inlet boundary condition was set at the liquid surface. This condition takes into account the mass burning rate per unit area, which can be calculated as

$$m'' = \frac{V\rho}{At} \quad (28)$$

where  $A$  is the surface area of one-meter pool fire,  $A = \pi D^2/4 = 0.785 \text{ (m}^2\text{)}$ ,  $V$  is the volume of ethanol,  $\rho$  is the ethanol density,  $t$  is the burning time. In this work, the mass burning rate per unit area was calculated on the basis of experimental data (Table 3).

Table 4 also compares the experimental and literature mass burning rates per unit area. The maximum difference between these results is 33%. There are several possible explanations for this finding. Note that the literature value refers to steady-state burning in quiescent environment in a tray without excessive lip height (Babrauskas, 1983). On the other hand, our experimental results cover all stages of a fire, and were obtained under a gentle wind.

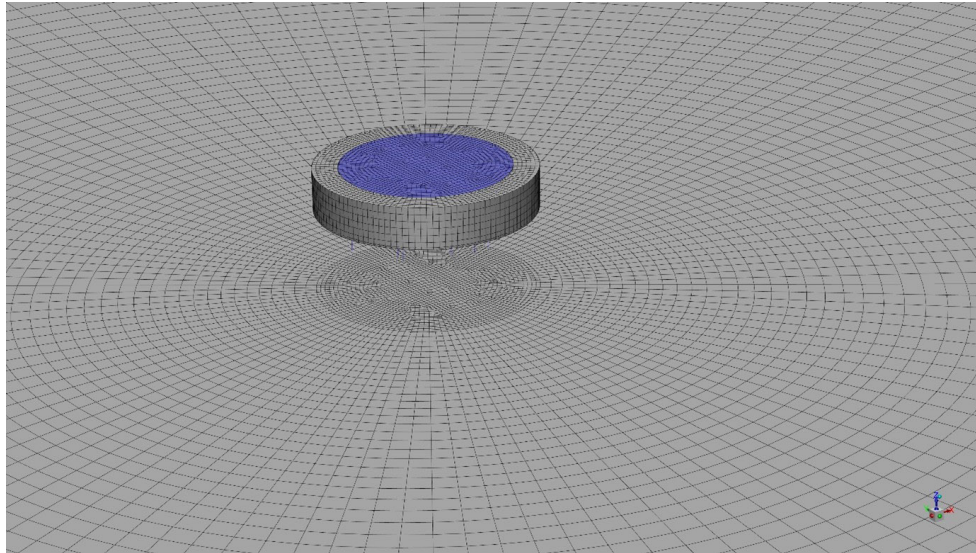


Fig. 5. Part of the computational mesh containing a one-meter test tray with ethanol (blue)

Table 4. Comparison of the calculated and literature mass burning rate per unit area

Run number	Volume of ethanol $V$ [dm <sup>3</sup> ]	Ethanol density, $\rho$ $\left[\frac{\text{kg}}{\text{m}^3}\right]$	Burning time $t$ [s]	Experimental mass burning rate per unit area $m''$ $\left[\frac{\text{kg}}{\text{m}^2\text{s}}\right]$	Literature mass burning rate per unit area (Babrauskas, 1983) $m''_{\text{lit}}$ $\left[\frac{\text{kg}}{\text{m}^2\text{s}}\right]$	Difference [%]
Test 1	9.0	734.6	808	0.011	0.015	27
Test 2	9.0	734.6	856	0.011		27
Test 3	9.0	734.6	869	0.010		33

The pressure outlet boundary condition was set at the top and sides of the computational domain, while the wall boundary condition was applied to the ground and walls of the test tray.

The problem was solved using unsteady calculations. In our CFD simulations, a fixed time step of 0.00025 s was used. The choice of such a time step guaranteed the convergence of calculations.

According to Lin et. al. (2010) the ratio of characteristic flame diameter,  $D^*$ , and the computational grid size,  $dx$ , should be  $D^*/dx \geq 13$  (for the CFD predicted flame height to be independent of grid resolution).

$$D^* = \left( \frac{\dot{Q}}{\rho_a c_p T_a \sqrt{g}} \right)^{\frac{2}{5}} \quad (29)$$

where:  $\dot{Q}$  is the total heat release rate ( $\dot{Q} = Am''\Delta H_{\text{combust}}$ ),  $T_\infty$  is the ambient temperature,  $g$  is the acceleration due to gravity,  $c_p$  is the specific heat of air at constant pressure,  $\rho_\infty$  is the ambient density.

Assuming the values:  $T_a = 293$  K,  $g = 9.81$  m/s<sup>2</sup>,  $c_p = 1.0$  kJ/(kg K),  $\rho_a = 1.2$  kg/m<sup>3</sup>,  $\Delta H_c = 26\,800$  kJ/kg (heat of ethanol combustion), the characteristic flame diameter is equal to  $D^* = 0.516$  m for the one-meter ID test tray.

The grid size used in the simulation was 2.96 cm, which is safely below the threshold value of 3.97 cm resulting from  $D^*/dx \geq 13$ . Consequently, we assumed that our results were mesh-independent.

To summarize the theoretical part, all the assumptions and models used in the CFD simulations are shown in Table 5.

Table 5. The models and assumptions used in the CFD simulations

	Balance equation/ modelled phenomenon/ model	Assumption or simplification	Reference
Governing equations	Momentum balance • Turbulence: Stress-Blended Eddy Simulation (SBES) model		ANSYS Inc. (2021)
	Species transport equation • Combustion: Eddy Dissipation model	The rate of combustion is infinitely fast, i.e. fuel reacts immediately after mixing with an oxidant	Magnussen and Hjertager (1977)
	Energy balance • Thermal radiation: Discrete Ordinate model		ANSYS Inc. (2021)
Mass burning rate	–	Calculated from Eq. (28), not directly measured	This work
Flame height	–	The flame tip is at the height at which 99% of the fuel is consumed	Ma and Quintiere (2003) McGrattan et al. (2012)
Geometry	–	Ethanol fills the inside of the tray and the liquid surface is at the edge of the tray	This work
	–	The CFD predicted flame height is independent of grid resolution when the ratio of characteristic flame diameter, $D^*$ , and the computational grid size, $dx$ , is $D^*/dx \geq 13$	Lin et. al. (2010)

#### 4. RESULTS AND DISCUSSION

This section compares the CFD and experimental results with respect to temperature measured in three axial locations above the test tray, the flame height and the centreline values of the mean excess temperature. Moreover, the radiative fraction (ratio of the radiative and total heat release rates) and the maximum axial temperature were compared with the literature.

The instantaneous and mean velocity and temperature fields calculated for ethanol pool fire on a 1 meter test tray are shown in Figures 6 and 7, respectively.

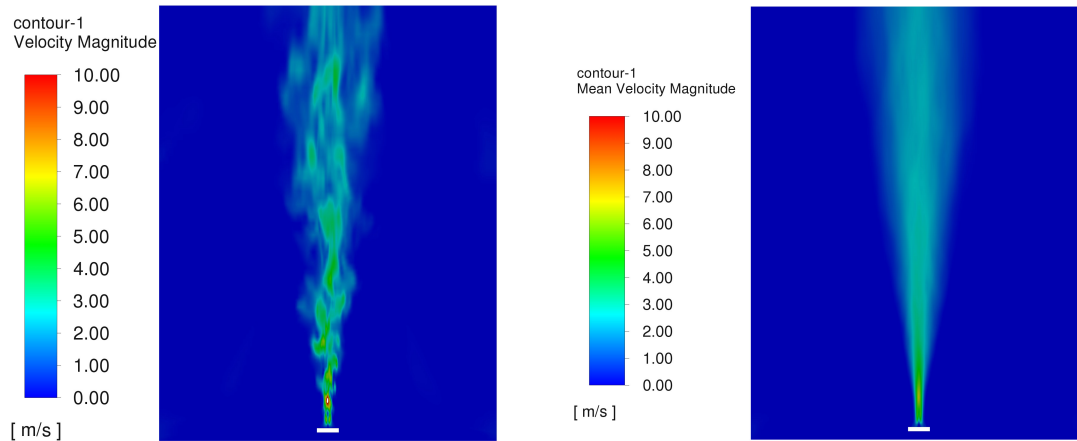


Fig. 6. The instantaneous (left) and mean (right) velocity fields calculated for ethanol pool fire on a 1 meter test tray

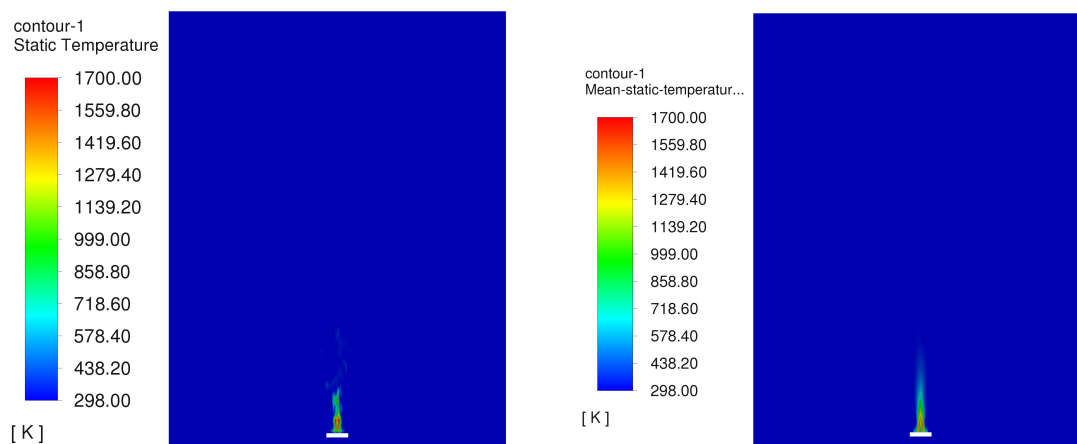


Fig. 7. The instantaneous (left) and mean (right) temperature fields calculated for ethanol pool fire on a 1 meter test tray

Figure 8 shows the axial mean experimental temperatures above the test tray. Note that the error bars represent standard deviations as the experiments were repeated three times.

Although three experiments were performed with the same volume of ethanol, one of them (test 2, Table 2) was excluded from further analysis as the obtained results were unreliable, possibly due to a strong change in wind speed. The reproducibility of the other experimental results is rather good, as evidenced by the standard deviations in Figure 8. Some discrepancy was expected given that the studies were conducted in an open space. It is clear from the results that wind gusts had some impact on the course of the pool fire tests despite the fact that the measurements were carried out at low average wind speeds (0.4 m/s). Note also that there is another likely reason for such performance. It is likely that a steady state was not reached during these tests. There are several reasons for that: (1) change of the heat conduction losses into the liquid, (2) presence of edge heating effects, (3) progressive heating of the bottom of the tray when the fuel layer is thin, (4) change of convective and radiative fluxes due to lip effects (Babrauskas, 1983). In addition, it is reported that ten minutes or even more may sometimes be required before fully steady-state is reached (Babrauskas, 1983). Taken together, it is proposed that the whole time frame of 600 s can be divided into three stages:

- 1) the fire growth – between 0 s and 100 s,
- 2) the fully developed fire – between 100 s and ~ 220 s, and
- 3) the fire decay – between ~ 220 s and 600 s. As a consequence, only the fully developed fire phase was used to compare the experimental and CFD results.

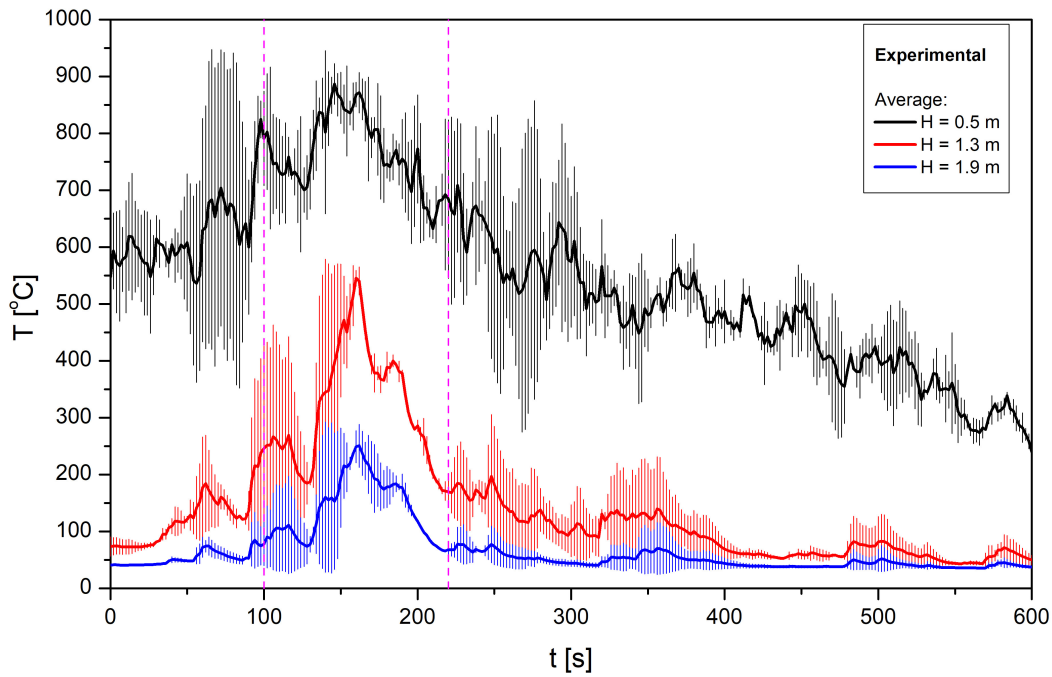


Fig. 8. The axial experimental temperatures for the ethanol pool fire above a 1 meter test tray. The solid vertical lines denote standard deviations. The dashed magenta lines between 100 s and ~ 220 s indicate the phase of a fully developed fire

Taking into account that the wind gusts most likely disturbed the flames, the temperature profiles shown in Fig. 8 were smoothed in the range from 100 s to 220 s using the Savitzky–Golay method (OriginLab Corporation, 2021). Second order local polynomial regression was applied to remove noise without disturbing the overall shape of the temperature profiles (Fig. 9).

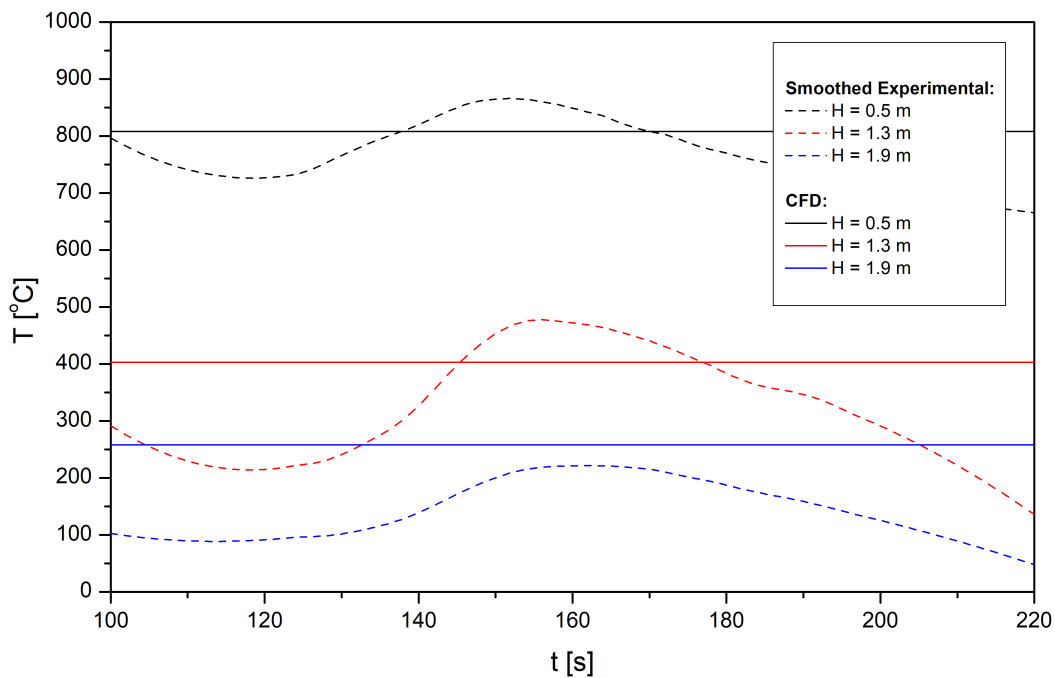


Fig. 9. Comparison of the calculated and experimental axial temperatures over a 1 meter test tray for ethanol pool fire. The experimental profiles were smoothed using the Savitzky–Golay method

Note that apart from some discrepancy observed at 1.9 m above the tray, there is a satisfactory quantitative and excellent qualitative agreement between the results of experiments and modelling. Moreover, our CFD

results are consistent with previous experimental results (Falkenstein-Smith et al., 2021) showing data for methanol, ethanol, and acetone pool fires in a quiescent environment. Although our and literature distributions of axial temperatures above the ethanol pool fire cannot be directly compared due to the different pool fire diameters (0.3 m in Falkenstein-Smith et al. (2021) and 1 m in this work), the maximum temperatures match quite well (1281 K in Falkenstein-Smith et al. (2021) compared to 1364 K in this work).

The radiative heat release rate (RHRR) was calculated in this work as follows:

$$\dot{Q}_r = 2\pi R_t \int_{Z_{\text{ethanol}}}^{Z_{\text{max}}} I(R_t, z) dz \quad (30)$$

where  $R_t$  is the radius of the test tray (the inner chamber filled with ethanol),  $I$  is the surface incident radiation (net incoming radiation heat flux on a surface),  $Z_{\text{ethanol}}$  is the height of the ethanol surface equal to the edge of the tray,  $Z_{\text{max}}$  is the height of the computational domain.

The radiative fraction was calculated by normalization of RHRR with the total fire heat release rate, showing the 14% share of thermal radiation. This is in fairly good agreement with earlier experimental results that showed the 17% and 20% radiative fractions for the ethanol pool diameters of 7.1 cm and 4.6 cm, respectively (Gore et al., 2007). A similar result, showing the 21% radiative fraction (with the 26% measurement uncertainty) was reported for the ethanol pool diameter of 0.301 m (Chan Kim et al., 2019).

Apart from comparing temperatures and thermal radiation, CFD simulation results can be verified by comparing flame heights that were recorded during experiments and determined from numerical simulations. In experiments, the flame intermittency is frequently used for that purpose. Using this criterion, the mean flame height is defined as the distance above fire where the intermittency is equal to 0.5, which means that the flame spends the same fraction of time above and below this characteristic height. On the other hand, CFD simulations require the introduction of an appropriate criterion to determine the flame height. One of the methods is the concept of chemical flame height which was introduced by Newman and Wieczorek (2004). According to this idea, the chemical flame height is defined using the ratio of CO to CO<sub>2</sub> yields approaching the limit for a well-ventilated fire. Given that the results obtained with this concept were in perfect functional agreement with the authors' previous luminous flame height correlations, chemical flame height was proposed to quantify the luminous flame height for well ventilated diffusion flames of surface fires. In the present work, we estimated the flame height using the criterion of 99% fuel consumption that assumes that the flame tip is at the height at which 99% of the fuel is consumed (Ma and Quintiere, 2003; McGrattan et al., 2012). Using this criterion, the flame height was detected as the maximum vertical position of isosurface for a constant fuel mass fraction value of 0.01. Flame heights can also be calculated from the classical Heskestad and Thomas correlations. Namely, in the method proposed by Heskestad (2016), flame height is calculated according to Equation (31).

$$H_f = 0.235\dot{Q}^{2/5} - 1.02D \quad (31)$$

where  $\dot{Q}$  is the total heat release rate, and  $D$  is the pool fire diameter.

In turn, according to the Thomas equation (Thomas, 1963), flame height is calculated as follows

$$H_f = 42 D \left( m'' / \rho_a \sqrt{gD} \right)^{0.61} \quad (32)$$

where  $m''$  is the mass burning rate of fuel per unit surface area,  $\rho_a$  is the ambient air density,  $D$  is the pool fire diameter,  $g$  is the acceleration due to gravity.

Figure 10 compares flame heights obtained from CFD simulations and estimated from experiments as well as calculated from the Heskestad and Thomas correlations.

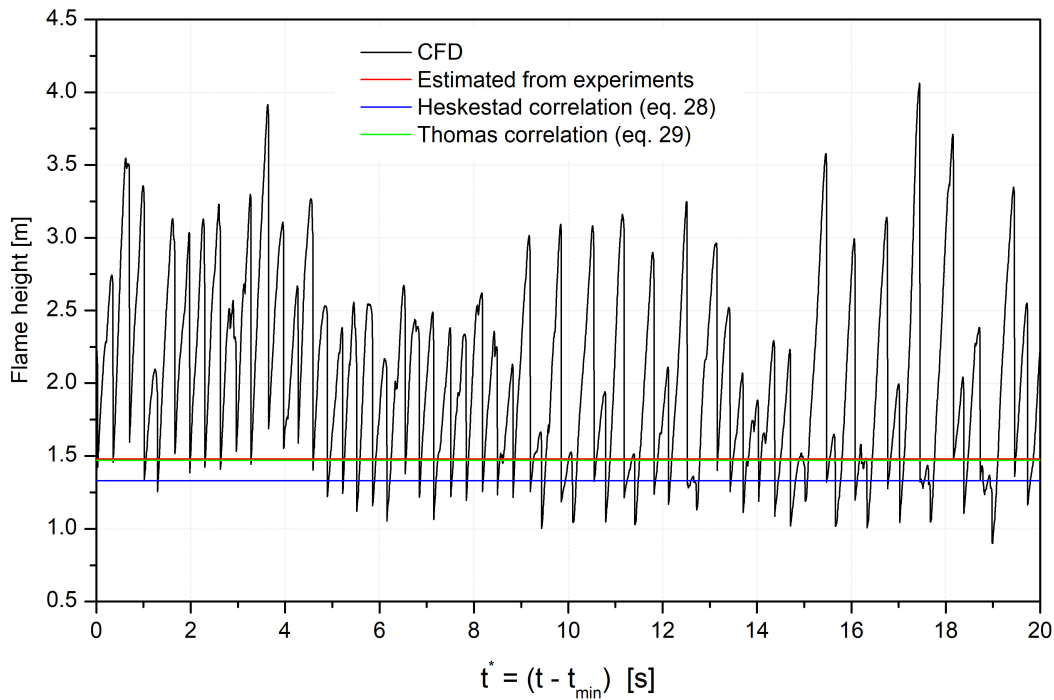


Fig. 10. Comparison of the experimental and calculated flame heights for the ethanol pool fire on a 1 meter test tray

It can be seen in Fig. 10 that there is an exceptional agreement between the experiments and Thomas correlation and a good match between the experiments and Heskestad correlation. This is not unexpected given the fact that the flame heights in the performed experiments and the used correlations were determined on the basis of the same intermittency criterion. On the other hand, the flame heights computed with the CFD model are on average higher. This is because the criterion of 99% fuel consumption was used in the computations in order to establish flame height at each time step. This criterion arbitrarily determines the flame height in the CFD model. Clearly, introducing a slightly different fuel consumption threshold as this criterion, for example 95%, would probably reduce the flame height. Regardless of the flame height criterion itself, another aspect which could impact our calculation's result is the lip effect. While the pool fire experiments were carried out with the test tray partially filled with ethanol, the CFD model adopted the simplification that the fuel surface was at the same height as the edge of the tray (tray completely filled with fuel). Note that one of the reported lip effects is an increase of turbulence near the base of the flame, which results in a shorter flame (Babrauskas, 1983; Steinhaus et al., 2007). Hence, it is likely that this effect is also reflected in our CFD calculation results, regardless of the criterion used to determine the flame height.

The results of CFD simulations can also be validated using the plume centreline values of mean excess temperature, which can be calculated using the following widely recognized equation (Heskestad, 2016).

$$\Delta T_0 = 9.1 \left( \frac{T_a}{g c_p^2 \rho_a^2} \right)^{1/3} \dot{Q}_c^{2/3} (z - z_0)^{-5/3} \quad (33)$$

where:  $T_a$  is the ambient temperature,  $g$  is the acceleration due to gravity,  $c_p$  is the specific heat of air at constant pressure,  $\rho_a$  is the ambient density (values assumed in this work  $T_a = 293$  K,  $g = 9.81$  m/s<sup>2</sup>,  $c_p = 1.00$  kJ/kg K,  $\rho_a = 1.2$  kg/m<sup>3</sup>),  $\dot{Q}_c$  is the convective heat release rate (assumed in this work  $\dot{Q}_c/\dot{Q} = 0.7$ , Heskestad, 2016),  $z$  is the elevation above the base of fire,  $z_0$  is the elevation of virtual origin above the fire source.

The height of virtual origin was calculated as follows (Heskestad, 2016)

$$\frac{z_0}{D} = -1.02 + 0.083 \frac{\dot{Q}^{2/5}}{D} \quad (34)$$

where  $D$  is the diameter of pool fire,  $\dot{Q}$  is the total heat release rate, which was calculated as

$$\dot{Q} = m'' \Delta H_c A \quad (35)$$

where  $m''$  is the mass burning rate per unit area obtained from Eq. (28),  $\Delta H_c$  is the heat of combustion of the fuel,  $A = \pi D^2/4$  is the pool fire area.

Table 6 highlights the height of virtual origin and the total heat release rate obtained for the ethanol pool fire on a one-meter test tray.

Table 6. The calculated values the total heat flux and the elevation of virtual origin above the fire source for ethanol pool fire on a one-meter test tray

Variable	Value	Equation No.
$z_0$ , m	-0.287	(34)
$\dot{Q}$ , kW	232	(35)

Using the data presented in Table 6, the plume centreline values of mean excess temperature were calculated with Eq. (33) and then compared with the temperature profile obtained from the CFD simulations.

Note that Equation (33) was derived from different plume theories which consider the plume zone above the flames. As a consequence, this equation is not valid in the flame zone. On the other hand, CFD simulations make it possible to find a temperature distribution in both zones: plume and flame. Overall, the profiles presented in Fig. 11 can only be compared in the plume zone above the flames, where almost a perfect

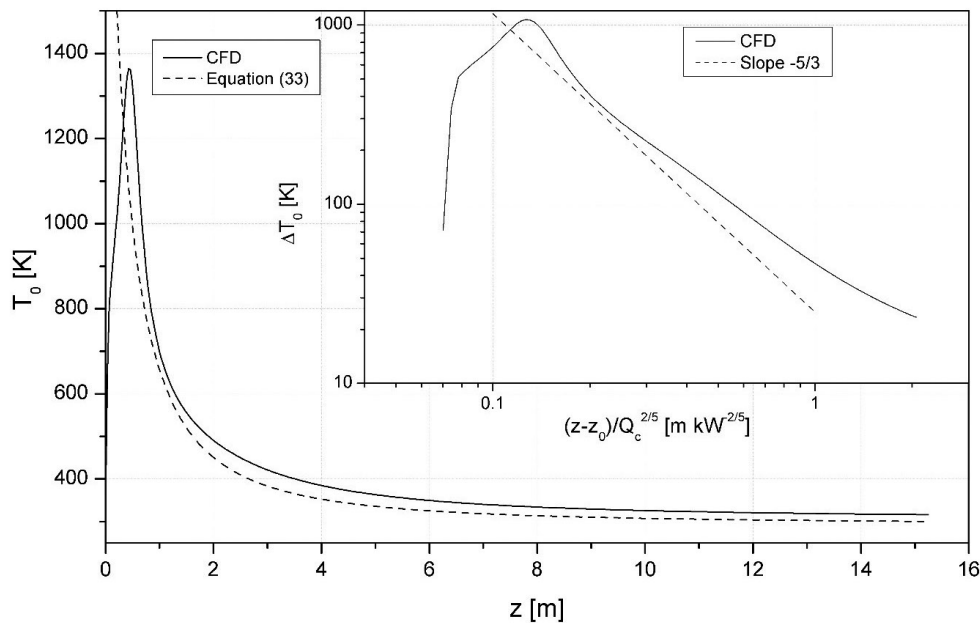


Fig. 11. Comparison of the centreline values of mean excess temperature (above ambient) calculated for the ethanol pool fire on a 1 meter test tray by using CFD and Eq. (33). The inset graph: Temperature rise on the plume centreline of pool fires after linearization of Eq. (33)

match of the profiles can be observed. When plotting  $\Delta T_0$  versus  $(z - z_0)/\dot{Q}_c^{2/5}$  in logarithmic coordinates, the centreline temperature rise should decrease with the  $-5/3$  product of the abscissa as follows from the following transformation of Equation (33).

$$\lg(\Delta T_0) = \frac{1}{3} \lg\left(9.1 \frac{T_a}{g c_p^2 \rho_a^2}\right) - \frac{5}{3} \lg\left(\frac{z - z_0}{\dot{Q}_c^{2/5}}\right) \quad (36)$$

As shown in the inset in Figure 10, the results of the CFD calculations plotted in the transformed coordinates agree well with the plume law for temperature (33) according to which the slope of the curve is  $-5/3$ .

While our CFD results are fairly in line with the experimental and literature results, there is certainly room for improvement. It is plausible that a number of limitations may have influenced the results obtained. The first concerns the mass burning rate per unit area that was calculated as the average value based on experimental fuel mass and the burning time from Eq. (28) and not measured directly as the instantaneous value. Another possible source of error is the uncertainty of the temperature measurements due to the possible influence of thermal radiation on the temperature measurement by N-type thermocouples.

## 5. CONCLUSIONS

Following the introduced new targets for renewable energy source consumption by 2030, together with an increased 14% sub-target for transport, the storage volume of ethanol will significantly increase. As a result, the ethanol fire hazard should be considered as a potential risk with a high probability of occurrence.

A mathematical model was proposed for ethanol pool fire on a one-meter test tray. The balance equations of mass, momentum, energy together with the combustion model were solved using CFD technique in 3D geometry. A relatively new hybrid RANS-LES model (SBES) was used to calculate turbulent stresses. The model allowed to obtain results consistent with the experiment with lower computational costs and shorter computation time compared to the classic but demanding LES model. The obtained CFD results were compared with our experimental results concerning flame heights and flame temperatures at different elevations. They were also verified against literature data for radiative fraction and various theoretical expressions for flame height and the centreline values of mean excess temperature. Testing of the CFD model showed good matching with the results of experiments and theoretical predictions (flame height, temperature rise on the plume centreline). A comparison of the measured flame temperatures at three elevations above the test tray with the CFD results revealed some discrepancy only for the highest thermocouple (1.9 m above the tray). The flame heights computed with the CFD model were on average higher than the experimental one. However, this is due to the assumed criterion of 99% fuel consumption, which was used to determine flame height in our CFD simulations. With regard to the centreline values of mean excess temperature, almost a perfect match of the CFD and theoretical (calculated from the plume law for temperature) profiles was observed.

The current study was mostly limited by two factors: (1) the uncertainty of the temperature measurements due to the possible influence of thermal radiation on the temperature measurement by N-type thermocouples, and (2) the mass burning rate per unit area that was calculated as the average value based on experimental fuel mass and the burning time from Eq. (28) and not directly measured. Nevertheless, we believe our work could be the basis for future work which might include investigations taking into account more detailed geometry of the tray's edge, variability of boundary conditions (variable burning rate, influence of wind etc.).

The publication was prepared under the project no. DOB-BIO7/09/03/2015 entitled “Risk Assessment Toolbox at Hazardous Industrial Facilities Posing Threat Outside their Area” financed by the National Centre for Research and Development.

## SYMBOLS

$A$	surface area, $m^2$
$A, B$	empirical constants
$c_p$	specific heat at constant pressure, $J/(kg \cdot K)$
$dx$	grid size, m
$D$	domain
$D$	mass diffusion coefficient, $m^2/s$
$D$	pool fire diameter, m
$D^*$	characteristic flame diameter, m
$D_{T,j}$	thermal diffusion coefficient, $kg/(m \cdot s)$
$E$	total energy, $J/kg$
$f_{SBES}$	blending function
$\vec{F}$	external body force, $kg/(m^2 \cdot s^2)$
$F_1, F_2, F_3$	functions containing six parameters: $C_{SEP}$ , $C_{MIX}$ , $C_{NW}$ , $C_{JET}$ , $C_{CORNER}$ and $C_{CURVE}$
$\vec{g}$	gravitational acceleration, $m/s^2$
$G$	filtering function
$h$	enthalpy, $J/kg$
$H_f$	flame height, m
$\Delta H_c$	heat of combustion, $kJ/kg$
$I$	radiation intensity, energy per area of emitting surface per unit solid angle
$I$	surface incident radiation (net incoming radiation heat flux on a surface), $W/m^2$
$\vec{J}$	mass diffusion in turbulent flow, $kg/(m^2 \cdot s)$
$k$	conductivity, $W/(m \cdot K)$
$k$	turbulence kinetic energy, $J/kg$
$m''$	mass burning rate per unit area, $kg/(m^2 \cdot s)$
$p$	static pressure, Pa
$\dot{Q}$	total heat release rate, W
$\dot{Q}_c$	convective heat release rate, W
$\vec{r}$	position vector, m
$R_t$	radius of the test tray, m
$R$	net rate of production by combustion, $kg/(m^3 \cdot s)$
$\vec{s}$	direction vector
$\vec{s}'$	scattering direction vector
$S_h$	internal source of heating, $W/m^3$
$Sc_t$	turbulent Schmidt number
$S_{ij}$	strain rate tensor, $1/s$
$S_m$	source term in the mass balance, $kg/(m^3 \cdot s)$
$t$	time, s
$T$	temperature, K
$\vec{v}$	velocity vector, $m/s$
$V$	volume, $m^3$
$Y$	mass fraction
$z$	elevation above the base of fire, m
$z_0$	elevation of virtual origin above the fire source, m

$Z$	height of the ethanol surface equal to the edge of the tray, m
$Z_{\max}$	height of the computational domain, m

*Greek symbols*

$\alpha$	absorption coefficient, 1/m
$\eta$	instantaneous value of velocity components or pressure, m/s or kg/(m·s <sup>2</sup> )
$\eta'$	fluctuating value of velocity components or pressure, m/s or kg/(m·s <sup>2</sup> )
$\bar{\eta}$	mean value of velocity components or pressure, m/s or kg/(m·s <sup>2</sup> )
$\mu$	viscosity, kg/(m·s)
$\rho$	density, kg/m <sup>3</sup>
$\sigma_s$	scattering coefficient, 1/m
$\bar{\bar{\tau}}$	stress tensor, N/m <sup>2</sup>
$\bar{\varphi}$	filtered variable
$\Phi$	phase function
$\Omega$	solid angle
$\sigma$	Stefan–Boltzmann constant, W/(m <sup>2</sup> ·K <sup>4</sup> )
$\varphi$	quantity to be filtered
$\omega$	specific turbulence kinetic energy dissipation rate, W/kg

*Superscripts*

LES	Large Eddy Simulation
SBES	Stress-Blended Eddy Simulation
RANS	Reynolds-averaged Navier–Stokes

*Subscripts*

a	ambient
eff	effective
$j$	species $j$
lit	literature
$m$	mixture
$P$	product
$R$	reactant
$T$	thermal
$t$	turbulent

## REFERENCES

- ANSYS Inc., 2021. *Ansys Fluent User's Guide. Release 2021 R2*. ANSYS, Inc. Canonsburg, USA.
- Attar A.A., Pourmahdian M., Anvaripour B., 2013. Experimental study and CFD simulation of pool fires. *Int. J. Comput. Appl.*, 70, 9–15. DOI: [10.5120/12004-5790](https://doi.org/10.5120/12004-5790).
- Babrauskas V., 1983. Estimating large pool fire burning rates. *Fire Technol.*, 19, 251–261. DOI: [10.1007/BF02380810](https://doi.org/10.1007/BF02380810).
- Brushlinsky N., Ahrens M., Sokolov S., Wagner P., 2020. *World Fire Statistics, Report No. 25*. CTIF World Fire Statistics Center. Available at: [https://www.ctif.org/sites/default/files/2020-06/CTIF\\_Report25.pdf](https://www.ctif.org/sites/default/files/2020-06/CTIF_Report25.pdf)
- Cajot L.G., Haller M., Pierre M., 2008. *Projektowanie Konstrukcji Stalowych Zespolonych z Uwzględnieniem Warunków Pożarowych*, DIFISEK. Poznań, 1–36 (in Polish).
- Calvo Olivares R.D., Rivera S.S., Núñez Mc Leod J.E., 2015. Database for accidents and incidents in the fuel ethanol industry. *J. Loss Prev. Process Ind.*, 38, 276–297. DOI: [10.1016/j.jlp.2015.10.008](https://doi.org/10.1016/j.jlp.2015.10.008).

- Chan Kim S., Lee K.Y., Hamins A., 2019. Energy balance in medium-scale methanol, ethanol, and acetone pool fires. *Fire Saf. J.*, 107, 44–53. DOI: [10.1016/j.firesaf.2019.01.004](https://doi.org/10.1016/j.firesaf.2019.01.004).
- Chotzoglou K.E., Asimakopoulou E.K., Zhang J., Delichatsios M.A., 2019. An experimental investigation of burning behaviour of liquid pool fire in corridor-like enclosures. *Fire Saf. J.*, 108, 102826. DOI: [10.1016/j.firesaf.2019.102826](https://doi.org/10.1016/j.firesaf.2019.102826).
- Directive 2009/28/EC of the European Parliament and of the Council of 23 April 2009 on the promotion of the use of energy from renewable sources and amending and subsequently repealing Directives 2001/77/EC and 2003/30/EC. *OJ L*, 140, 5.6.2009, 16. DOI: [10.3000/17252555.L\\_2009.140.eng](https://doi.org/10.3000/17252555.L_2009.140.eng).
- Ebrahim Zadeh S., Beji T., Merci B., 2016. Assessment of FDS 6 simulation results for a large-scale ethanol pool fire. *Combust. Sci. Technol.*, 188, 571–580. DOI: [10.1080/00102202.2016.1139367](https://doi.org/10.1080/00102202.2016.1139367).
- Falkenstein-Smith R., Sung K., Chen J., Hamins A., 2021. Chemical structure of medium-scale liquid pool fires. *Fire Saf. J.*, 120, 103099. DOI: [10.1016/j.firesaf.2020.103099](https://doi.org/10.1016/j.firesaf.2020.103099).
- Fenimore C.P., Jones G.W., 1967. Oxidation of soot by hydroxyl radicals. *J. Phys. Chem.*, 71, 593–597. DOI: [10.1021/j100862a021](https://doi.org/10.1021/j100862a021).
- Fischer S.J., Hardouin-Duparc B., Grosshandler W.L., 1987. The structure and radiation of an ethanol pool fire. *Combust. Flame*, 70, 291–306. DOI: [10.1016/0010-2180\(87\)90110-6](https://doi.org/10.1016/0010-2180(87)90110-6).
- Gore J., Klassen M., Hamins A., Kashiwagi T., 2007. Fuel property effects on burning rate and radiative transfer from liquid pool flames, In: Cox G., Langford B. (Eds.), *Fire Safety Science — Proceedings of the Third International Symposium*. Taylor & Francis, London, New York. 359-404. DOI: [10.4324/9780203973493](https://doi.org/10.4324/9780203973493).
- Hakkarainen T., Korhonen T., Vaari J., 2021. Fire safety of alcoholic beverages in retail stores. *Fire Mater.*, 45, 1044-1050. DOI: [10.1002/fam.2956](https://doi.org/10.1002/fam.2956).
- Hamins A., Klassen M., Gore J., Kashiwagi T., 1991. Estimate of flame radiance via a single location measurement in liquid pool fires. *Combust. Flame*, 86, 223–228. DOI: [10.1016/0010-2180\(91\)90102-H](https://doi.org/10.1016/0010-2180(91)90102-H).
- Heskestad G., 2016. Fire plumes, flame height, and air entrainment, In: Hurley M.J., Gottuk D., Hall J.R., Harada K., Kuligowski E., Puchovsky M., Torero J., Watts J.M., Wiecek C. (Eds.), *SFPE Handbook of fire protection engineering*. Springer, New York, NY. 396–428. DOI: [10.1007/978-1-4939-2565-0\\_13](https://doi.org/10.1007/978-1-4939-2565-0_13).
- Khan I.M., Greeves G., 1974. A method for calculating the formation and combustion of soot in diesel engines. In: Afgan N.H., Beer J.M. (Eds.), *Heat transfer in flames*. Scripta Book Co., Washington.
- Lee K.B., Thring M. W., Beer J. M., 1962. On the rate of combustion of soot in a laminar soot flame. *Combust. Flame*, 6, 137–145. DOI: [10.1016/0010-2180\(62\)90082-2](https://doi.org/10.1016/0010-2180(62)90082-2).
- Lin C.H., Ferng Y.M., Hsu W.S., Pei B.S., 2010. Investigations on the characteristics of radiative heat transfer in liquid pool fires. *Fire Technol.*, 46, 321–345. DOI: [10.1007/s10694-008-0071-7](https://doi.org/10.1007/s10694-008-0071-7).
- Ma T.G., Quintiere J.G., 2003. Numerical simulation of axi-symmetric fire plumes: accuracy and limitations. *Fire Saf. J.*, 38, 467–492. DOI: [10.1016/S0379-7112\(02\)00082-6](https://doi.org/10.1016/S0379-7112(02)00082-6).
- Magnussen B.F., Hjertager B.H., 1977. On mathematical modeling of turbulent combustion with special emphasis on soot formation and combustion. *Symp. (Int.) Combust.*, 16, 719–729. DOI: [10.1016/S0082-0784\(77\)80366-4](https://doi.org/10.1016/S0082-0784(77)80366-4).
- Maragkos G., Merci B., 2021. Grid insensitive modelling of convective heat transfer fluxes in CFD simulations of medium-scale pool fires. *Fire Saf. J.*, 120, 103104. DOI: [10.1016/j.firesaf.2020.103104](https://doi.org/10.1016/j.firesaf.2020.103104).
- Marlair G., Rotureau P., Breulet H., Brohez S., 2009. Booming development of biofuels for transport: Is fire safety of concern? *Fire Mater.*, 33, 1–19. DOI: [10.1002/fam.976](https://doi.org/10.1002/fam.976).
- McGrattan K., McDermott R., Floyd J., Hostikka S., Forney G., Baum H., 2012. Computational fluid dynamics modelling of fire. *Int. J. Comput. Fluid Dyn.*, 26, 349–361. DOI: [10.1080/10618562.2012.659663](https://doi.org/10.1080/10618562.2012.659663).
- Newman J.S., Wiecek C.J., 2004. Chemical flame heights. *Fire Saf. J.*, 39, 375–382. DOI: [10.1016/j.firesaf.2004.02.003](https://doi.org/10.1016/j.firesaf.2004.02.003).
- OriginLab Corporation, 2021. *Origin Help. Smoothing*. Available at: <https://www.originlab.com/doc/origin-help/smoothing>.

- Rengel B., Mata C., Pastor E., Casal J., Planas E., 2018. A priori validation of CFD modelling of hydrocarbon pool fires. *J. Loss Prev. Process Ind.*, 56, 18–31. DOI: [10.1016/j.jlp.2018.08.002](https://doi.org/10.1016/j.jlp.2018.08.002).
- Schälike S., Wehrstedt K.D., Gawlowski M., Schönbacher A., 2012. Validation of submodels for CFD simulation of n-hexane pool flames including interferometry. *Chem. Ing. Tech.*, 84, 484–490. DOI: [10.1002/cite.201100179](https://doi.org/10.1002/cite.201100179).
- Sjöström J., Amon F., Appel G., Persson H., 2015a. Thermal exposure from large scale ethanol fuel pool fires. *Fire Saf. J.*, 78, 229–237. DOI: [10.1016/j.firesaf.2015.09.003](https://doi.org/10.1016/j.firesaf.2015.09.003).
- Sjöström J., Appel G., Amon F., Persson H., 2015b. *ETANKFIRE – Experimental results of large ethanol fuel pool fires*. SP Technical Research Institute of Sweden. Borås.
- Snegirev A., Markus E., Kuznetsov E., Harris J., Wu T., 2018. On soot and radiation modeling in buoyant turbulent diffusion flames. *Heat Mass Transfer*, 54, 2275–2293. DOI: [10.1007/s00231-017-2198-x](https://doi.org/10.1007/s00231-017-2198-x).
- Steinhaus T., Welch S., Carvel R.O., Torero J.L., 2007. Large-scale pool fires. *Therm. Sci.*, 11, 101–118. DOI: [10.2298/TSCI0702101S](https://doi.org/10.2298/TSCI0702101S).
- Stewart J.R., Phylaktou H.N., Andrews G.E., Burns A.D., 2021. Evaluation of CFD simulations of transient pool fire burning rates. *J. Loss Prev. Process Ind.*, 71, 104495. DOI: [10.1016/j.jlp.2021.104495](https://doi.org/10.1016/j.jlp.2021.104495).
- Tesner P.A., Snegiriova T.D., Knorre V.G., 1971. Kinetics of dispersed carbon formation. *Combust. Flame*, 17, 253–260. DOI: [10.1016/S0010-2180\(71\)80168-2](https://doi.org/10.1016/S0010-2180(71)80168-2)
- Thomas P.H., 1963. The size of flames from natural fires. *Symp. (Int.) Combust.*, 9, 844–859. DOI: [10.1016/S0082-0784\(63\)80091-0](https://doi.org/10.1016/S0082-0784(63)80091-0).

Received 25 December 2021

Received in revised form 22 February 2022

Accepted 25 February 2022